RSC Advances

PAPER

View Article Online
View Journal | View Issue

Cite this: *RSC Adv.*, 2025, **15**, 35617

Comparative evaluation of amoxicillin loading and release behavior from waste-derived hydroxyapatite synthesized by solid-state and wet chemical routes

Mashrafi Bin Mobarak, *[a] Sumaya Tabassum, [a] Md Sohag Hossain, [a] Nourin Tarannum, [b] Fariha Chowdhury, [c] Md. Sahadat Hossain, [a] Nazmul Islam Tanvir[d] and Samina Ahmed *[a]

This study presents a comparative analysis of amoxicillin loading and release behaviors of hydroxyapatite (HAp) synthesized by two methods, solid-state reaction (S-HAp1000) and wet chemical precipitation (W-HAp1000) using waste chicken eggshells as the calcium source and calcination at 1000 °C for 2 hours. Structural and morphological characterization revealed significant differences: S-HAp1000 exhibited a biphasic composition with 75.5% HAp and 24.5% β-TCP based on Rietveld refinement, larger crystallite size (88 nm), and higher amoxicillin entrapment efficiency (11.63%), while W-HAp1000 exhibited 99.6% phase-pure HAp, smaller crystallite size (83 nm), and lower entrapment efficiency (7.28%). Drug release in simulated body fluid (SBF) at pH 7.4 and 4.0 showed that W-HAp1000 released 62.96% and 79.18% of amoxicillin respectively, compared to 44.66% and 66.01% for S-HAp1000. Release kinetics revealed that amoxicillin release from S-HAp1000 followed an anomalous (non-Fickian) transport mechanism at physiological pH (7.4), which shifted toward a diffusion-controlled (Fickian) mechanism under acidic conditions (pH 4.0). In contrast, W-HAp1000 exhibited a concentration-dependent, zero-order release profile at pH 7.4, transitioning to a case II transport mechanism, characterized by matrix relaxation or erosion at pH 4.0. W-HAp1000 also showed broader antibacterial activity, inhibiting both *S. aureus* and *E. coli*, whereas S-HAp1000 was only effective against *S. aureus*. These findings suggest that synthesis methodology significantly influences the drug delivery performance of HAp for osteomyelitis therapy.

Received 14th August 2025
Accepted 21st September 2025

DOI: 10.1039/d5ra06021d

rsc.li/rsc-advances

1 Introduction

Hydroxyapatite (HAp), a naturally occurring calcium phosphate compound with the chemical formula $Ca_{10}(PO_4)_6(OH)_2$, is the principal mineral component of bone and teeth, making it one of the most widely studied biomaterials in the field of biomedical engineering.[1–3] Its excellent biocompatibility, osteoconductivity, and similarity to the inorganic matrix of human hard tissues make it highly suitable for bone regeneration, orthopedic implants, dental materials, and drug delivery systems.[4–7] HAp can be synthesized from a wide variety of calcium sources, including chemical precursors such as, $CaCO_3$, $Ca(NO_3)_2$, $CaCl_2$, *etc.* and biological waste materials such as eggshells, seashells, and fish bones, which makes it a sustainable and economical choice for biomedical applications.[8] Among the various synthetic approaches, HAp can be prepared through solid-state reaction, wet chemical precipitation, sol–gel methods, hydrothermal treatment, and biomimetic processes.[9–12] The properties of HAp such as crystallinity, particle size, surface area, and phase purity are heavily influenced by the synthesis conditions, including temperature, pH, precursor ratio, and calcination protocol.[13] Owing to its high surface activity and tunable physicochemical properties, HAp has gained increasing attention as a matrix for loading and delivering therapeutic agents, especially antibiotics for localized treatment of bone infections.[14–16]

It is well-documented that the synthesis method used for preparing HAp significantly affects its final structural, morphological, and functional characteristics. Solid-state synthesis, typically involving mechanical mixing and high-temperature calcination, produces highly crystalline materials but often leads to secondary phase formation, such as β-tricalcium phosphate (β-TCP), due to incomplete homogenization

[a]*Institute of Glass and Ceramic Research and Testing (IGCRT), Bangladesh Council of Scientific and Industrial Research (BCSIR), Dhaka-1205, Bangladesh. E-mail: mashrafibinmobarak@gmail.com; shanta_samina@yahoo.com*

[b]*Institute of Technology Transfer and Innovation (ITTI), Bangladesh Council of Scientific and Industrial Research (BCSIR), Dhaka-1205, Bangladesh*

[c]*Biomedical and Toxicological Research Institute (BTRI), Bangladesh Council of Scientific and Industrial Research (BCSIR), Dhaka-1205, Bangladesh*

[d]*BCSIR Dhaka Laboratories, Bangladesh Council of Scientific and Industrial Research (BCSIR), Dhaka-1205, Bangladesh*

at the atomic scale.[13,17] On the other hand, wet chemical precipitation offers superior control over stoichiometry and particle morphology through solution-based reactions, yielding phase-pure HAp with finer particles and greater surface homogeneity.[18] These variations can directly influence the performance of HAp in applications such as drug delivery, where parameters like crystallinity, porosity, and surface chemistry govern the drug loading capacity and release kinetics.[7,19] The choice of synthesis method of HAp is also crucial as it influences the *in vivo* performance. For instance, the wet chemical method typically yields HAp with smaller crystallite size and higher surface area, which are crucial for promoting osteoinduction during bone regeneration.[20] This synthesis route is also favorable for better biodegradation rate and ensuring resorbability of the scaffold as the new bone tissue forms.[21,22] On the other hand, solid-state method with better thermal stability and crystallinity, often results in HAp with a slower biodegradation rate. The presence of a secondary, more resorbable β-tricalcium phosphate phase in the solid-state synthesized HAp could mitigate this effect, but the overall greater crystallinity of the material still suggests a more stable structure compared to the nanocrystalline HAp from the wet chemical route.[23,24] Therefore, a systematic comparison of HAp synthesized by different methods is essential for tailoring its performance in specific biomedical applications. This study aims to evaluate the influence of two common synthetic routes, solid-state and wet chemical precipitation on the drug delivery behavior of HAp, with a focus on amoxicillin as the model drug.

Bone-related infections, including osteomyelitis, present a serious clinical challenge due to their chronic nature and resistance to conventional systemic antibiotic treatments.[25] Targeted drug delivery using bone-mimicking carriers like HAp offers a promising alternative by ensuring localized, sustained release of antibiotics directly at the infection site, thereby minimizing systemic side effects and enhancing therapeutic efficacy.[26] Amoxicillin, a broad-spectrum β-lactam antibiotic, is widely used for treating infections caused by *Staphylococcus aureus*, a key pathogen implicated in osteomyelitis. Its mechanism of action involves inhibiting bacterial cell wall synthesis, making it highly effective against Gram-positive bacteria.[27,28] However, to achieve optimal efficacy, especially in localized infections, amoxicillin must be delivered in a controlled and sustained manner. HAp, owing to its high affinity for phosphate-based antibiotics and bioactive nature, serves as an excellent matrix for amoxicillin delivery. Evaluating the drug loading and release performance of HAp prepared *via* different synthesis methods is therefore highly relevant for advancing therapeutic strategies in bone infection management.

In this work, a comparative study was undertaken to investigate the impact of synthesis methodology on the drug loading and release behavior of HAp derived from waste chicken eggshells. Two distinct approaches were employed: a high-temperature solid-state method (S-HAp1000) and a wet chemical precipitation method (W-HAp1000). Chicken eggshell was utilized as the source of Ca. The resulting samples were characterized using a suite of techniques including XRD, FTIR, Raman spectroscopy, FESEM, TEM, and DLS to identify structural and morphological differences. Subsequently, the samples were evaluated for their amoxicillin loading efficiency, *in vitro* drug release kinetics under physiological and acidic pH conditions, and antibacterial performance against *Staphylococcus aureus* and *Escherichia coli*. This study not only explores how synthetic methodology shapes the physicochemical properties of HAp, but also how these variations affect its function as a drug delivery platform, particularly in the context of localized bone infection treatment.

2 Materials and methods

2.1. Materials

The pivotal raw material used in this experiment was waste chicken eggshell which was collected from different food shops of University of Dhaka. White shells of chicken egg were mostly present in the waste. These shells are a huge source of Ca (94–97%) which is normally present as $CaCO_3$.[19] Diammonium hydrogen phosphate ($(NH_4)_2HPO_4$) and phosphoric acid (H_3PO_4) were procured from Merck, Germany and ammonia solution (NH_4OH) was procured from Scharlau, Spain. Amoxicillin was procured from Merck, India. De-ionized water (DI) was used in all solution preparations.

2.2. Methods

2.2.1. Processing of chicken eggshells into powder. The collected waste chicken eggshells were washed to remove dirt. Then, they were boiled at 100 °C for an hour to harden the inner membrane, making it easier to remove. After that, the eggshells were dried in an oven at 105 °C to remove moisture. Once dried, they were ground in a ball mill (MTI Corporation, model: MSK-SFM-1) at 450 rpm for 2 hours.

2.2.2. Solid-state preparation of hydroxyapatite. The solid-state preparation of HAp was carried out by following our previously reported technique.[9,13,29] Based on the theoretical ratio of Ca/P as 1.67, a 20 g of waste chicken eggshell powder was mixed with 15 g of $(NH_4)_2HPO_4$ in an alumina pot where 16 yttrium stabilized ZrO_2 balls of different diameter were added for milling purposes. Two pots with the same amounts of ingredients and balls were placed at opposite positions of the ball mill and the milling operation was continued for 6 hours at 450 rpm. Once milled, the powdered mixture was placed in a ceramic dish and subjected to calcination at 1000 °C at a heating rate of 10 °C per minute for 2 hours. The calcined sample was labelled as S-HAp1000 and stored in air tight conditions.

2.2.3. Wet chemical preparation of hydroxyapatite. At first, 20 g of powdered eggshell was subjected to calcination at 900 °C at a heating rate of 5 °C per minute for 60 minutes in order to convert the $CaCO_3$ into CaO. This heat treatment process also helps in the removal of organic contaminants from the eggshell.[19] Considering the theoretical ratio of Ca/P as 1.67, a 5.6 g of freshly prepared CaO was weighed, placed in a beaker, mixed with 100 mL of DI water and stirred for 60 minutes in order to convert the CaO into $Ca(OH)_2$ which is made sure by the evolution of heat as this is an exothermic reaction. In the just

prepared $Ca(OH)_2$ solution, 0.6 M 100 mL H_3PO_4 solution was slowly added dropwise by maintaining constant magnetic stirring condition. White precipitate of calcium phosphate started to appear with the addition of phosphoric acid. Once the addition completed, stirring was continued for half an hour and then NH_4OH was used to reach the pH of the solution to 11. Stirring was maintained during pH adjustment and continued for an additional 4 hours afterward. The solution was kept overnight at static condition for aging and the total procedure was carried out at room temperature. The white precipitate was separated by vacuum filtration and subjected to oven drying at 105 °C for several hours until constant weight. The dried sample was hand-ground by mortar and pestle, followed by calcination at 1000 °C at a heating rate of 10 °C per minute for 2 hours. The calcined sample was labelled as W-HAp1000 and stored in airtight conditions. The synthesis scheme of S-HAp1000 and W-HAp1000 is illustrated in Fig. 1.

2.2.4. Methods used for characterization. The prepared S-HAp1000 and W-HAp1000 samples were subjected to instrumental characterization techniques such as X-ray powder diffractometry (XRD) (Rigaku Smart Lab XRD, CuKα radiation = 1.54060 Å, operation at 40 kV and 50 mA). Search and match operation was carried out by X'Pert HighScore Plus software and Rietveld refinement was done by Profex 5.4.1. package. Morphology analysis was done by both Field Emission Scanning Electron Microscopy (FESEM) (JEOL JSM-7610F) and Transmission Electron Microscopy (TEM) (Talos F200X G2). Elemental analysis was carried out by Energy Dispersive X-ray spectroscopy (EDS) with the aid of FESEM and TEM instrumentation. Fourier-transform infrared spectroscopy (FTIR) (MIRacle10 ATR- IR Prestige21) and Raman spectroscopy (HORIBA Macro-RAM) helped in functional group analysis. UV-Visible absorption measurements were taken by Hitachi U-2910 spectrophotometer.

2.2.5. Formulation of simulated body fluid (SBF) solution. For the comparative study of *in vitro* amoxicillin release from the prepared HAp samples, a metastable buffer solution, also called SBF, was prepared according to the procedure reported by Tas.[30] This procedure is an alteration of the previously reported procedure of Kokubo *et al.*[31] We also implemented this technique for SBF preparation in our previous study.[7,19] The most significant change in Tas's method is the increased concentration of bicarbonate ion (HCO_3^-) from 4.2 mM to 27 mM which fixes the deficiency problem in traditional methods. Additionally, the chloride ion (Cl^-) concentration was reduced from 147.8 mM to 125 mM, as human blood plasma contains only 103 mM of Cl^- ions. Table 1 reports the chemicals, their purity and amount used for the preparation of SBF solution (pH 7.4) in this study compared to Tas's procedure.

2.2.6. Drug release assessment in SBF solution. Before assessing the release of amoxicillin from the synthesized S-HAp1000 and W-HAp1000 samples, the drug was first loaded onto the materials. A 100-ppm stock solution of amoxicillin was prepared in DI water. For drug loading, 250 mg of each sample

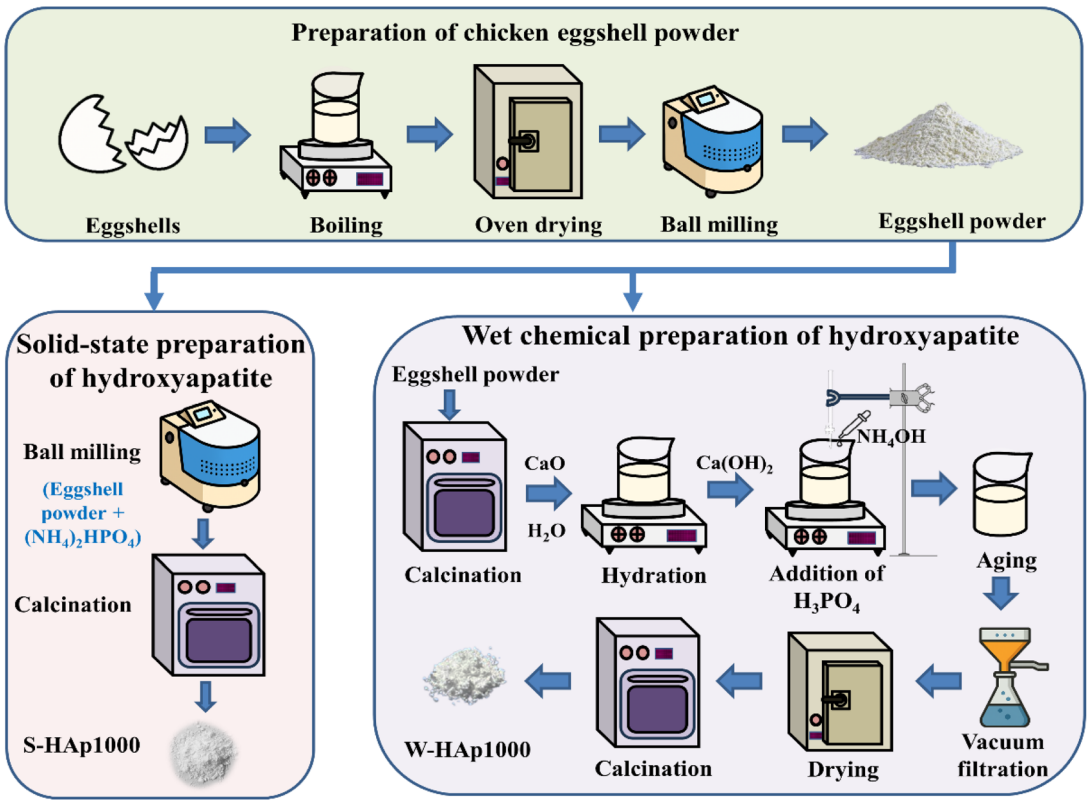

Fig. 1 Synthesis scheme of HAp, starting with chicken eggshell waste followed by preparation by solid-state and wet chemical precipitation routes.

Table 1 List of chemicals used for the preparation of SBF solution at 37 °C

Order of addition	Chemical name, formula and molecular weight ($g\ mol^{-1}$)	Country of origin and purity	Amount used in the method of Tas[30]	Amount used for this study
1	Sodium chloride (NaCl); 58.44	Merck Germany; 99.5%	6.547	6.5456
2	Sodium bicarbonate ($NaHCO_3$); 84.01	Merck Germany; 99.5%	2.268	2.2671
3	Potassium chloride (KCl); 74.55	Merck Germany; 99.5%	0.373	0.370
4	Disodium phosphate (Na_2HPO_4); 156.01	Merck Germany; 98%	0.178	0.179
5	Magnesium chloride hexahydrate ($MgCl_2 \cdot 6H_2O$); 203.30	Merck Germany; 99%	0.305	0.3014
6	Calcium chloride dihydrate ($CaCl_2 \cdot 2H_2O$); 147.02	Merck Germany; 99.5%	0.368	0.3616
7	Sodium sulfate (Na_2SO_4); 142.04	Merck Germany; 99%	0.071	0.076
8	Tris(hydroxymethyl) aminomethane ($(CH_2OH)_3CNH_2$); 121.14	Scharlau Spain; 99.8%	6.057	6.054

was weighed separately into 100 mL beakers, followed by the addition of 50 mL of the amoxicillin solution. The mixtures were magnetically stirred at room temperature for 2 hours to ensure thorough adsorption.

After stirring, the amoxicillin-loaded samples were separated *via* vacuum filtration using a 0.2 μm microfilter. The collected samples were then dried at 60 °C for 3 hours. The absorbance of both the initial amoxicillin stock solution and the filtrates was measured at 228 nm using a UV-Vis spectrophotometer. A calibration curve ($R^2 = 0.9909$) was established using amoxicillin solutions of varying concentrations (2, 4, 6, 8, and 10 ppm) to determine the unknown concentrations.

The entrapment efficiency and loading capacity of the S-HAp1000 and W-HAp1000 samples for amoxicillin were calculated using the following equations.

$$\text{Entrapment efficacy}(\%) = \frac{\text{initial concentration of amoxicillin} - \text{concentration of amoxicillin in filtrate}}{\text{initial concentration of amoxicillin}} \times 100 \quad (1)$$

$$\text{Loading capacity}(\%) = \frac{\text{total amoxicillin encapsulated}}{\text{weight of carrier}} \times 100 \quad (2)$$

The release profile of amoxicillin from S-HAp1000 and W-HAp1000 samples was assessed in simulated body fluid (SBF) at two different pH levels (7.4 and 4.0) at RT. From the dried amoxicillin-loaded samples, 50 mg of each material was weighed, placed into conical flasks, and mixed with 25 mL of SBF (pH 7.4 or pH 4.0). The flasks were then placed in an orbital shaker set at 100 rpm at room temperature. At predetermined time intervals, 3 mL aliquots were withdrawn for UV absorbance measurements at 228 nm. Each withdrawn volume was immediately replaced with fresh SBF to maintain the total solution volume. Shaking was continued for 5 hours, and the cumulative release of amoxicillin from S-HAp1000 and W-HAp1000 at both pH conditions was calculated using the following equation.[7,19]

$$\text{Cumulative amoxicillin release}(\%) = \frac{\text{amount of amoxicillin in SBF solution}}{\text{initial amount of amoxicillin loaded on HAp samples}} \times 100 \quad (3)$$

2.2.7. Antibacterial activity assessment. The antibacterial activity of the amoxicillin loaded HAp samples was examined against *Staphylococcus aureus* (Gram-positive, ATCC 29737) and *Escherichia coli* (Gram-negative, ATCC 11229), following the agar-well diffusion technique, as outlined in previous studies.[32,33] In this method, sterile Mueller–Hinton Agar (MHA) medium (20–25 mL) was poured into 90 mm Petri dishes and left to solidify. An aliquot of 50 μL from freshly cultured bacterial suspensions ($\sim 10^5$ cells per 100 mL, $OD_{600} = 0.05$) was uniformly distributed over the agar surface using a sterile cotton swab. Wells of 6 mm diameter were created using

a sterile cork-borer, and 100 μL of various concentrations of the samples (ranging from 0.1 to 0.5 mg mL^{-1}) were carefully added. Tetracycline discs served as the positive control, while dimethyl sulfoxide (DMSO) was used as the solvent control. The prepared plates were incubated at 37 °C for 24 hours, and the diameters of inhibition zones were measured using a scale.[34]

2.2.7.1. MIC and MBC determination. The minimum inhibitory concentration (MIC) and minimum bactericidal concentration (MBC) of the samples against *Staphylococcus aureus* were evaluated *via* the broth microdilution method. The MIC and MBC determinations were conducted only against *Staphylococcus aureus*, as it is the primary causative agent of osteomyelitis.[19] Serial dilutions of the test solutions were prepared at concentrations ranging from 0.02 to 1.0 mg mL^{-1}. Fresh bacterial suspensions ($\sim 10^5$ cells per 100 mL, OD_{600} = 0.03–0.05) were cultured in Mueller–Hinton Broth (MHB) containing the different test concentrations and incubated at 37 °C for 24 hours. A bacterial suspension without test sample acted as the positive control, and MHB medium alone served as the negative control. After incubation, MIC and MBC were determined by comparing the turbidity of treated samples to the controls. Absorbance at 600 nm was recorded using a UV-Visible spectrophotometer to assess cell density.

2.2.7.2. Cytotoxicity assessment. The cytocompatibility of amoxicillin-loaded HAp samples was assessed using Vero cells (African green monkey kidney epithelial cell line).[35,36] Cells were cultured in DMEM supplemented with 10% fetal bovine serum and antibiotics, and seeded in 96-well plates (1.5×10^4 cells/100 μL). After 24 h incubation at 37 °C in 5% CO_2, 25 μL of 100 μg mL^{-1} for each sample was added, and cells were further incubated for 24 h. Viability was evaluated under a microscope and quantified using an automated cell counter. Cell viability (%) was calculated as the ratio of live to total cells × 100.

2.2.7.3. Statistical analysis. All experiments were independently performed in triplicate ($n = 3$). The results are presented as the mean ± standard deviation (SD).

3 Results and discussion

3.1. Powder X-ray diffraction (PXRD) analysis

The PXRD patterns of the synthesized S-HAp1000 and W-HAp1000 samples, shown in Fig. 2a, revealed differences in the phase compositions. For S-HAp1000, the diffraction peaks can be indexed to a biphasic system which comprises both HAp (matching ICDD file 01-074-0566) and β-tricalcium phosphate (β-TCP, matching ICDD file 00-009-0169) phases. The formation of β-TCP in the solid-state synthesis route can be attributed to localized non-stoichiometry and inhomogeneous mixing during ball milling, which introduce structural defects and Ca-deficient regions. Upon thermal treatment, these defects facilitate dehydroxylation and partial decomposition, resulting in β-TCP formation.[37] This biphasic nature is commonly observed in calcium phosphate ceramics synthesized by solid-state routes due to the lack of atomic-level mixing and the high-temperature calcination required for phase crystallization.[9,13,29] Rietveld refinement quantified the S-HAp1000 sample as consisting of 75.5% HAp and 24.5% β-TCP phases (Fig. 2b).

In contrast, the XRD pattern of W-HAp1000 showed well-defined peaks corresponding to HAp which matches closest to ICDD file 01-074-0565. The Rietveld refinement confirmed a phase purity of 99.6% HAp, with only 0.4% β-TCP detected. This superior phase purity is attributed to the solution-based wet chemical method, which ensures homogeneous mixing at the molecular level, precise control over stoichiometry and pH, and facilitated nucleation and growth of stoichiometric HAp crystals. The aging step further promotes crystallization and ordering, minimizing the formation of secondary phases even after high-temperature calcination.[38,39] The Rietveld-refined XRD patterns of the synthesized samples are presented in Fig. S1.

3.1.1. Analysis of crystallographic parameters. Assessment of crystallographic parameters is vital for grasping, as well as tuning the properties of a particular material for a specific application. For materials like HAp, crystallographic parameters influence its performance when subjected to a particular application.[7,9,40] Various crystallographic parameters of the synthesized HAp samples, such as lattice dimensions, volume and density of unit cell, relative intensity, preference growth, micro-strain, crystallite size, dislocation density, degree of crystallinity and crystallinity index were assessed and presented in Table 2.

The lattice parameters of the two HAp samples are nearly identical and consistent with standard ICDD reference data. The unit cell volume and density remained nearly the same for both samples, indicating structural consistency at the atomic level. However, differences were observed in microstructural features, where S-HAp1000 exhibited larger crystallite size compared to W-HAp1000. In contrast, the wet chemical method resulted in slightly higher microstrain and dislocation density, reflecting greater lattice imperfections likely due to lower-temperature processing steps prior to calcination. These imperfections also contributed to its lower degree of crystallinity compared to the solid-state HAp, indicating that the solid-state method produced more ordered and well-defined crystals. Additionally, the crystallinity index of both samples was close, showing that both methods yield reasonably crystalline materials, although the solid-state method yielded slightly better result in overall structural order. These differences indicates that the way HAp is synthesized can strongly affect its crystal structure, which may impact how well it works in drug delivery applications.

Another important crystallographic parameter for polycrystalline materials is texture coefficient (TC) which describes the preferred orientation of crystals. Preferred orientation refers to the alignment of crystals in a material such that certain crystallographic planes are more parallel than others, affecting XRD peak intensities and influencing properties like strength and bioactivity in materials like HAp.[41,42] TC is calculated using X-ray diffraction data by comparing the intensity of specific diffraction peaks in the sample to those in a standard reference. This comparison helps identify which crystallographic planes are more prominently aligned in the material, indicating a deviation from random orientation. Following equation was employed for calculating TC of the HAp samples.[43]

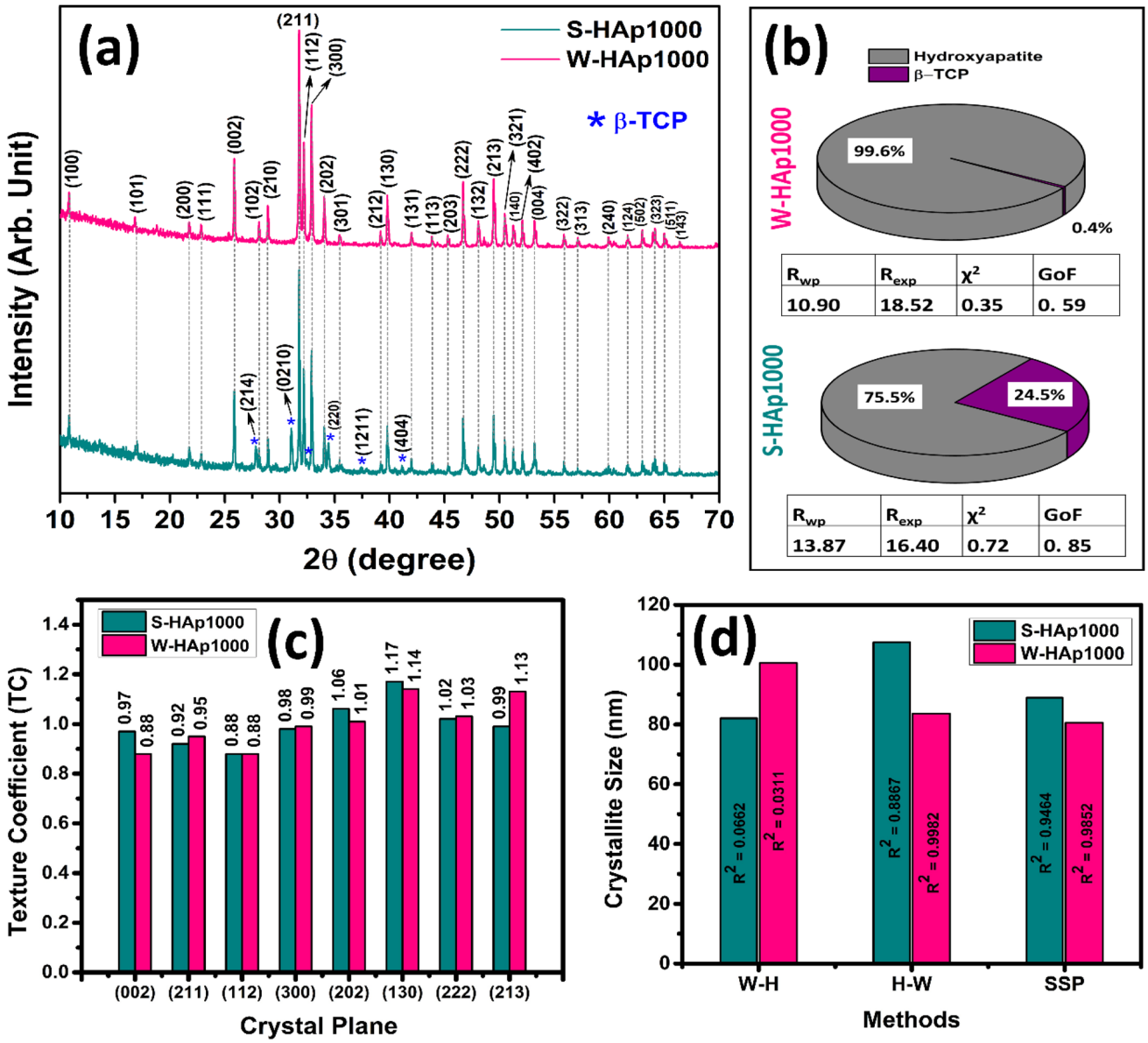

Fig. 2 (a) XRD patterns; (b) results of Rietveld refinement quantification; (c) comparative visualization of texture coefficients of selected planes; and (d) crystallite size calculation by Williamson–Hall (W–H), Halder–Wagner (H–W) and size-strain plot (SSP) methods, of the HAp samples prepared *via* solid-state and wet chemical method utilizing waste chicken eggshell as the precursor of Ca.

$$\mathrm{TC}_{(hkl)} = \frac{I_{\mathrm{sample}(hkl)} / I_{\mathrm{standard}(hkl)}}{\frac{1}{N}\sum_{n=1}^{N}\left(I_{\mathrm{sample}(hkl)} / I_{\mathrm{standard}(hkl)}\right)} \quad (4)$$

Here, $I_{\mathrm{sample}\ (hkl)}$ and $I_{\mathrm{standard}\ (hkl)}$ represents the measured and standard intensity of the (hkl) reflection and N is the total number of considered reflections. Calculation of preferred orientation of the selected crystallographic planes (planes with RI equal or greater than 20% were selected) for both HAp samples are presented in Table 3 and a comparative illustration is shown in Fig. 2c.

The TC values presented in Fig. 2c shows the preferential orientation of different crystallographic planes of HAp samples. Both samples exhibit non-random orientation across the measured planes, as indicated by TC values deviating from 1. Especially, for the S-HAp1000 sample, the (130) plane shows the highest TC which is the indication of a strong preferred growth along this direction. In contrast, the W-HAp1000 sample displays a slightly lower but still prominent TC for the same plane. Interestingly, the W-HAp1000 sample shows a higher TC than S-HAp1000 in the (213) plane, indicating a relatively stronger orientation preference along this plane. Essentially, the solid-state synthesized sample shows slightly more pronounced orientation in specific planes, which could contribute to improved structural properties.

The measured crystallite size of the HAp samples through Scherrer equation gives an indication that the crystallites are in the micro meter range. For microcrystalline materials, Scherrer

Table 2 Evaluation of crystallographic parameters of the synthesized HAp samples

Parameter	Mathematical expression with notation	Calculated and ICDD reference values			
		S-HAp1000	01-074-0566	W-HAp1000	01-074-0565
Lattice dimensions	$\frac{1}{d^2} = \frac{4}{3}\left(\frac{h^2+hk+k^2}{a^2}\right) + \frac{l^2}{c^2}$; d = inter-atomic layer distance; a, b, and c = dimensions of unit cell; h, k, and l = crystal plane representatives	$a = b = 9.4251$ Å, $c = 6.8838$ Å	$a = b = 9.4240$ Å, $c = 6.8790$ Å	$a = b = 9.4244$ Å, $c = 6.8844$ Å	$a = b = 9.4240$ Å, $c = 6.8790$ Å
Volume of unit cell (V)	$V = \frac{\sqrt{3}}{2}a^2c$	529.58 Å^3	529.09 Å^3	529.55 Å^3	529.09 Å^3
Density of unit cell (ρ)	$\rho = \frac{nA}{N_A V}$; n = number of atoms per unit cell; A = atomic weight of the molecule; N_A = Avogadro number (6.023×10^{23} mol^{-1})	3.15 g cm^{-3}	3.15 g cm^{-3}	3.15 g cm^{-3}	3.15 g cm^{-3}
Relative intensity (RI)	$\mathrm{RI}_{\mathrm{HAp}} = \frac{I_{(211)}}{I_{(300)} + I_{(112)} + I_{(002)}}$; $I_{(211)}$, $I_{(300)}$, $I_{(112)}$ and $I_{(002)}$ = intensities of corresponding crystal planes	0.64	1.06	0.69	1.06
Preference growth (P)	$P = \frac{\mathrm{RI}_{\mathrm{sample}} - \mathrm{RI}_{\mathrm{standard}}}{\mathrm{RI}_{\mathrm{standard}}}$; $\mathrm{RI}_{\mathrm{sample}}$ = RI of sample and $\mathrm{RI}_{\mathrm{standard}}$ = RI of standard value from ICDD PDF card	−0.40	—	−0.35	—
Microstrain (ε)	$\varepsilon = \frac{\beta}{4\tan\theta}$; β = full width half maxima; θ = diffraction angle	0.06	—	0.07	—
Crystallite size (D) by Scherrer equation	$D = \frac{k\lambda}{\beta\cos\theta}$; K = form factor (typically taken as 0.9); λ = wavelength of Cu Kα radiation (0.154060 nm for our instrument)	128.65 nm	—	102.45 nm	—
Dislocation density (δ), (nm^{-2}) $\times 10^{-5}$	$\delta = \frac{1}{D^2}$; D = crystallite size	6.04	—	9.53	—
Degree of crystallinity (X_C)	$X_c = \left(\frac{K_a}{\beta_{(211)}}\right)^3$; K_a = constant which is taken as 0.24; $\beta_{(211)}$ = FWHM of (211) plane	52.24	—	26.40	—
Crystallinity index (CI)	$\mathrm{CI} = \mathrm{CI}_{\mathrm{XRD}} = \sum \frac{H_{(300)} + H_{(112)} + H_{(002)}}{H_{(211)}}$; $H_{(300)}$, $H_{(112)}$, $H_{(002)}$ and $H_{(211)}$ = peak heights of corresponding crystal planes	1.52	—	1.49	—

Table 3 Calculation of texture coefficient of S-HAp1000 and W-HAp1000

Sample	Crystal plane	I_{sample} (*hkl*)	$I_{standard}$ (*hkl*)	$I_{sample\ (hkl)}/I_{standard\ (hkl)}$	Average, $\frac{1}{N}\sum_{n=1}^{N}(I_{sample(hkl)}/I_{standard(hkl)})$	Texture coefficient (TC)	Orientation (TC > 1 preferred TC < 1 suppressed TC = 1 random)
S-HAp1000	(002)	1058	35.7	26.64	$\frac{218.92}{8}=27.37$	0.97	Suppressed
	(211)	2520	100	25.20		0.92	Suppressed
	(112)	1238	51.5	24.04		0.88	Suppressed
	(300)	1645	61.3	26.84		0.98	Suppressed
	(202)	608	21.0	28.95		1.06	Preferred
	(130)	659	20.5	32.15		1.17	Preferred
	(222)	784	28.1	27.90		1.02	Preferred
	(213)	846	31.3	27.20		0.99	Suppressed
W-HAp1000	(002)	1116	35.3	31.61	$\frac{287.77}{8}=35.97$	0.88	Suppressed
	(211)	3406	100	34.06		0.95	Suppressed
	(112)	1640	52.0	31.54		0.88	Suppressed
	(300)	2164	60.9	35.53		0.99	Suppressed
	(202)	755	20.8	36.29		1.01	Preferred
	(130)	819	20.0	40.95		1.14	Preferred
	(222)	1042	28.1	37.08		1.03	Preferred
	(213)	1270	31.2	40.71		1.13	Preferred

equation alone is not sufficient because it neglects factors like microstrain and instrument-related peak broadening. To obtain a more accurate estimation of crystallite size, Williamson–Hall method (W–HM), Halder–Wagner method (H–WM) and size-strain plot method (SSPM) were also employed. The respective equations for these methods are as follows.

$$\beta\cos\theta = \frac{K\lambda}{D} + 4\varepsilon\sin\theta \quad (5)$$

$$\left(\frac{\beta}{\tan\theta}\right)^2 = \frac{K\lambda}{D}\times\frac{\beta\cos\theta}{\sin^2\theta} + 16\varepsilon^2 \quad (6)$$

$$(\mathrm{d}\beta\cos\theta)^2 = \frac{K\lambda}{D}\times\left(\mathrm{d}^2\beta\cos\theta\right) + \frac{\varepsilon^2}{4} \quad (7)$$

Linear fitting of the plots of $\beta\cos\theta$ *versus* $4\sin\theta$, $(\beta/\tan\theta)^2$ *versus* $(\beta\cos\theta/\sin^2\theta)$, and $(\mathrm{d}\beta\cos\theta)^2$ *versus* $\mathrm{d}^2\beta\cos\theta$ will result in intercept, slope, and slope equal to $K\lambda/D$, for W–HM, H–WM and SSPM, respectively. The linear fitted plots of these methods are presented in Fig. 3 and the comparative results are presented in Fig. 2d. Highest value of Coefficient of determination (R^2) was the basis of selecting the best suited method for selecting the crystallite size of the HAp samples. Based on this, S-HAp1000 and W-HAp1000 have crystallite size of 88 nm (SSPM with $R^2 = 0.9464$) and 83 nm (H-WM with $R^2 = 0.9982$).

3.2. Morphological analysis by FESEM and TEM techniques

The morphological analysis of the synthesized HAp samples reveals distinct differences in particle size, shape, and crystallinity as evidenced by FESEM and TEM analysis. For the S-HAp1000 sample, FESEM image (Fig. 4a) shows aggregated, irregularly shaped particles with a tendency to form clusters, which is typical of solid-state synthesis where mechanical grinding creates fractured surfaces and promotes particle clustering.[44] The particles were more of an irregular plate-like structures with overlapping edges and stacking.

At higher magnification (Fig. 4b), particles appear elongated and dense. The particle size histogram (Fig. 4c), obtained using ImageJ software, shows a broad distribution with an average particle size of 409 ± 150 nm (number of measured particles = 222), suggesting significant polydispersity. TEM images (Fig. 4d and e) confirm the dense, agglomerated nature of the particles. The corresponding selected area electron diffraction (SAED) pattern (Fig. 4f) shows a set of sharp diffraction rings, indicating polycrystalline nature, while the inset lattice fringe image confirms well-resolved lattice planes, indicative of good crystallinity after high-temperature calcination at 1000 °C.

On the other hand, the W-HAp1000 sample exhibits a finer and more homogeneous morphology. FESEM images (Fig. 4g and h) also displays plate-shaped particles, though they are smaller, thinner, and more uniformly distributed and less aggregated compared to the S-HAp1000. The particle size distribution (Fig. 4i) is narrower, with a smaller average size of 204 ± 87 nm (number of measured particles = 188), indicating a more uniform synthesis result *via* the wet chemical precipitation method. TEM analysis (Fig. 4j and k) further supports this observation, showing discrete particles with reduced aggregation. The average particle size from the TEM histogram is 158 ± 44 nm ($N = 31$), smaller than that of S-HAp1000 (284 ± 151 nm, $N = 49$). The SAED pattern (Fig. 4l) displays distinct diffraction rings similar to S-HAp1000, confirming polycrystalline nature. The lattice fringe image inset also indicates high crystallinity, although slightly less defined than S-HAp1000.

3.3. Elemental analysis by FESEM and TEM based EDX

Elemental analysis of the HAp samples was carried out by FESEM and TEM based EDX (Fig. 5). Both of the spectra confirm

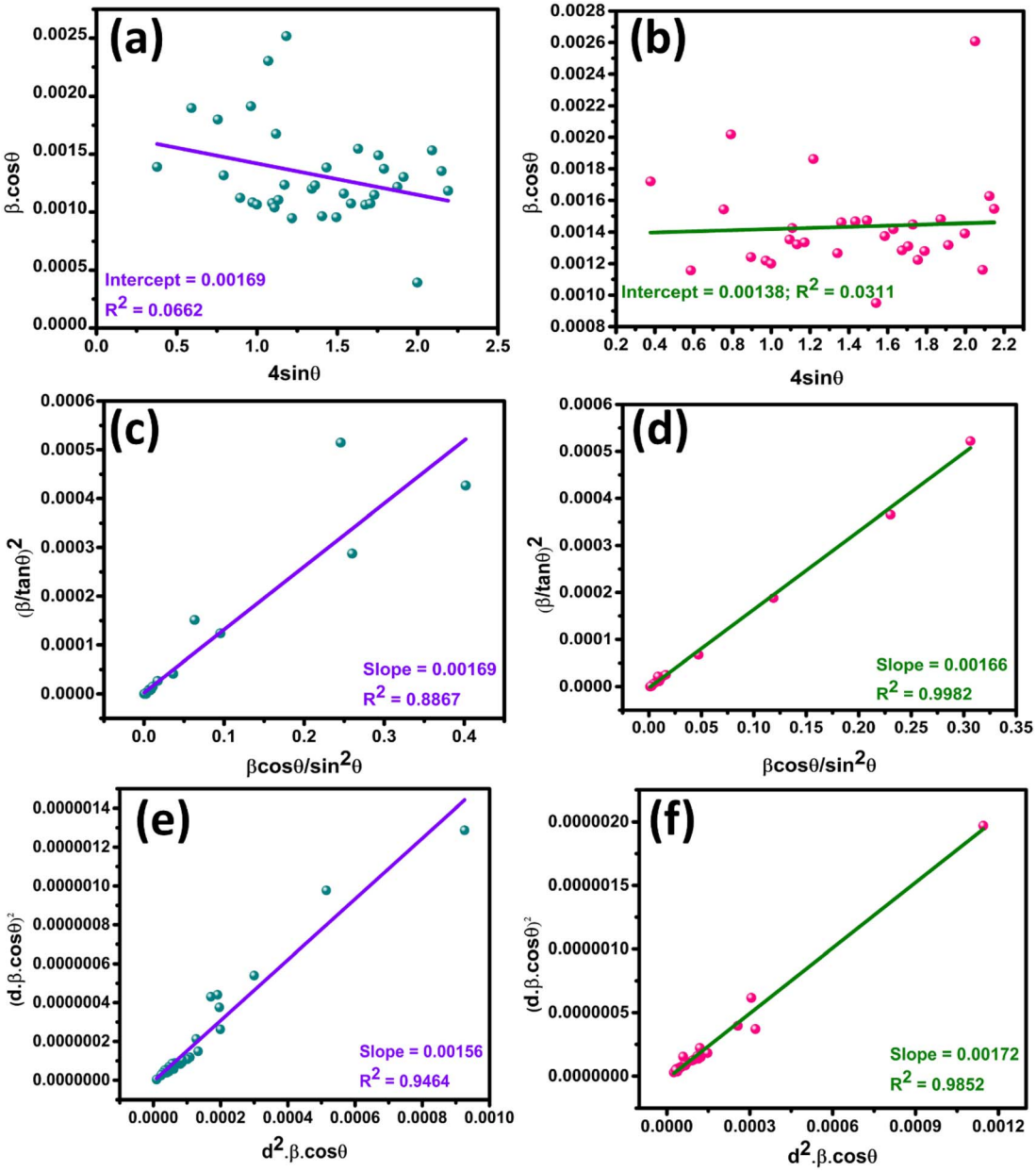

Fig. 3 Linear fitted plots for crystallite size measurements of S-HAp1000 and W-HAp1000 samples: (a and b) Williamson–Hall method (W–HM), (c and d) Halder–Wagner method (H–WM) and (e and f) size-strain plot method (SSPM).

the presence of Ca, P, and O, that are expected in HAp ($Ca_{10}(PO_4)_6(OH)_2$). In the FESEM-based EDX spectra, S-HAp1000 (Fig. 5a) shows Ca/P atomic ratio of 1.11, which is lower than the stoichiometric value of 1.67 for pure HAp. This suggests the presence of Ca-deficient apatite or partial carbonate substitution, which is common in biologically derived apatites.[19] In comparison, W-HAp1000 (Fig. 5b) showed a higher Ca/P ratio of 1.45 which indicates a relatively Ca-rich composition that may be attributed to the wet chemical synthesis process and higher incorporation of Ca^{2+} during precipitation.

The TEM-based EDX spectra also support the results of FESEM-based EDX. S-HAp1000 (Fig. 5c) exhibits significantly higher Ca and P contents with a Ca/P ratio of 1.38, whereas W-HAp1000 (Fig. 5d) yields Ca/P ratio of 1.57. This elevated ratio suggests greater lattice substitution or surface adsorption of Ca species, possibly influenced by the pH control and aging conditions in the wet chemical method.[18]

As observed from the elemental analysis by two different instrumental techniques, the wet chemical-derived HAp has the higher Ca/P ratio. A higher Ca/P ratio in HAp is often associated with improved thermal stability and lower solubility in physiological environments, which are beneficial for load-bearing biomedical applications and long-term implant integration.[45,46]

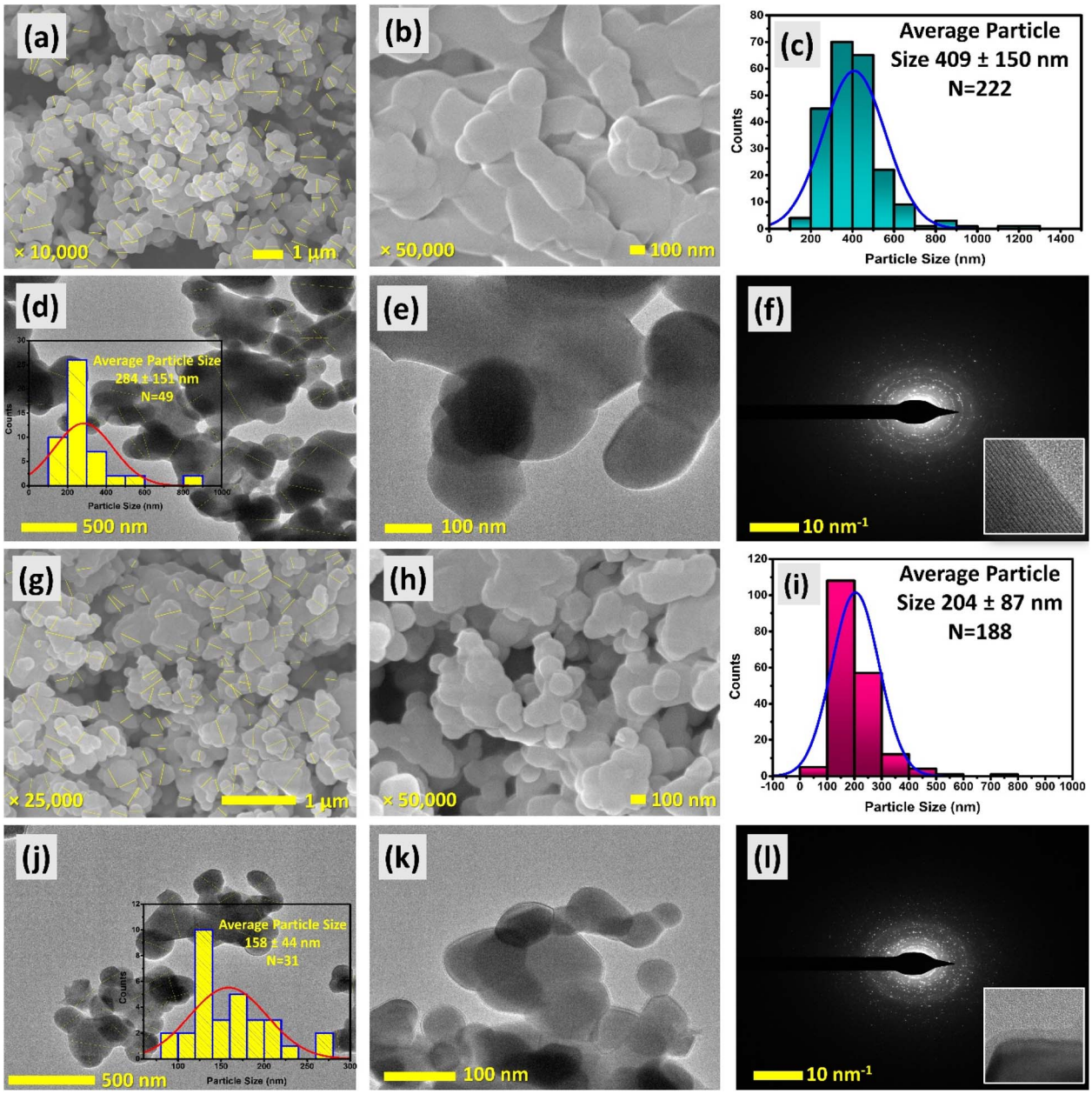

Fig. 4 Morphological analysis of the synthesized HAp samples: (a–c) FESEM and (d–f) TEM analysis of S-HAp1000 sample; (g–i) FESEM and (j–l) TEM analysis of W-HAp1000 sample.

3.4. Vibrational spectroscopic assessment of functional groups

The FTIR and Raman spectral analysis were employed for the assessment of functional groups that are present in the synthesized HAp samples. The analysis revealed the characteristic vibrational modes associated with phosphate group (PO_4^{3-}) that confirms the formation of HAp. In the FTIR spectra (Fig. 6a), both samples show prominent bands in the region of 1000–1100 cm^{-1} (at 1085 cm^{-1} and 1022–1024 cm^{-1}), corresponding to the asymmetric stretching vibrations (ν_3) of the PO_4^{3-} group.[35] Peak at 962 cm^{-1} is assigned to the symmetric stretching mode (ν_1) of PO_4^{3-} which also indicates well-crystallized HAp structure. Bending modes are observed near 600 cm^{-1} and 460 cm^{-1} which are typical of PO_4^{3-} groups. Specifically, asymmetric bending (ν_4) vibrations were observed at 599 cm^{-1} and 565 cm^{-1} for S-HAp1000, 597 cm^{-1} and 563 cm^{-1} for W-HAp1000. On the other hand, symmetric bending (ν_2) modes were observed at 459 cm^{-1} and 460 cm^{-1}, respectively.[47]

Meanwhile, vibrational bands for the structural –OH was observed at 3572 cm^{-1} and 628 cm^{-1} for both of the samples, indicating no shifts. Clear distinctions were observed for the S-HAp1000 sample with vibrational bands at 1408 cm^{-1} and 873 cm^{-1}, both of which indicates the presence of carbonate (CO_3^{2-}) group (B-type substitution).[48]

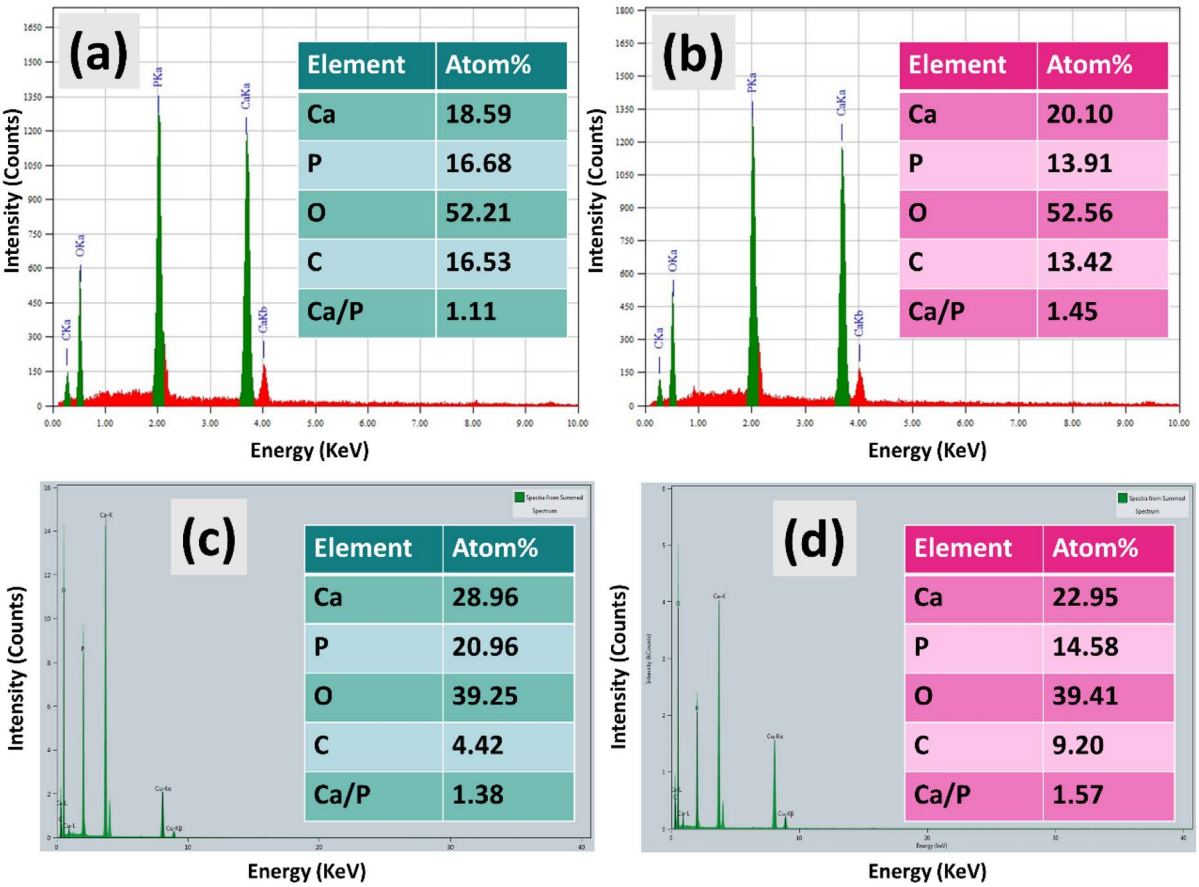

Fig. 5 Elemental analysis by FESEM and TEM based EDX: (a and c) S-HAp1000 and (b and d) W-HAp1000.

The Raman spectra (Fig. 6b) support the findings of FTIR analysis, with both samples displaying a strong and sharp band at 964 cm^{-1}. This Raman shift corresponds to the characteristic symmetric P–O stretching vibration (ν_1) of the PO_4^{3-} group, which is also a confirmatory band positions of HAp.[49] Triplet bending modes (ν_4) of PO_4^{3-} are observed at 576–618 cm^{-1}, while the lower frequency bands near 444–446 cm^{-1} are attributed to the symmetric O–P–O bending vibrations (ν_2). The peaks at 1046–1088 cm^{-1} correspond to the asymmetric stretching vibrations (ν_3) of PO_4.[3–13]

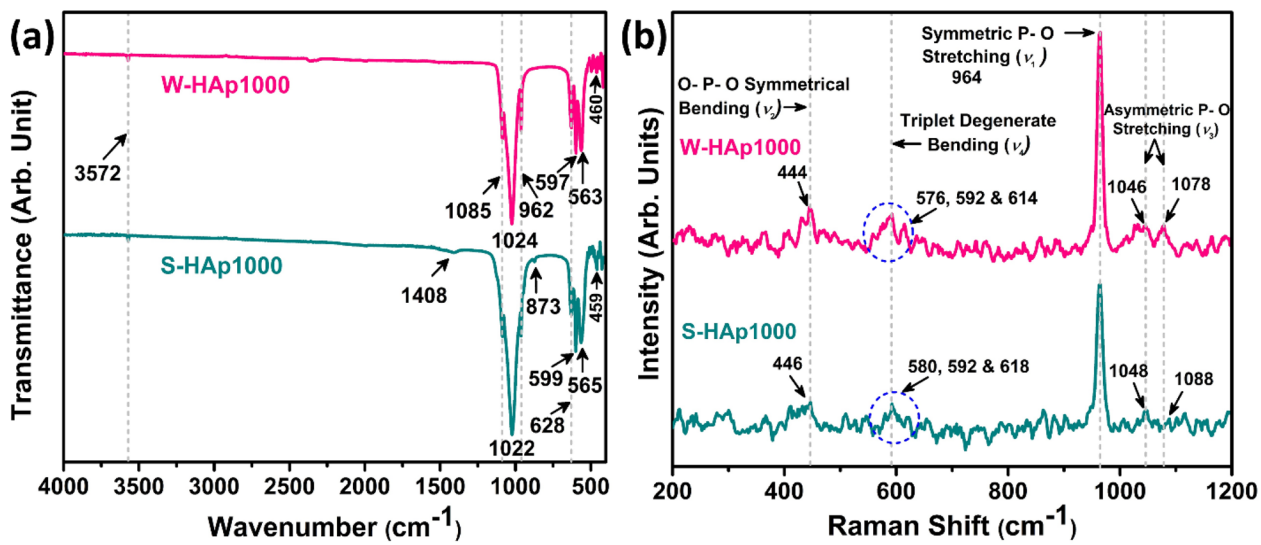

Fig. 6 (a) FTIR and (b) Raman spectroscopic analysis of the synthesized HAp samples.

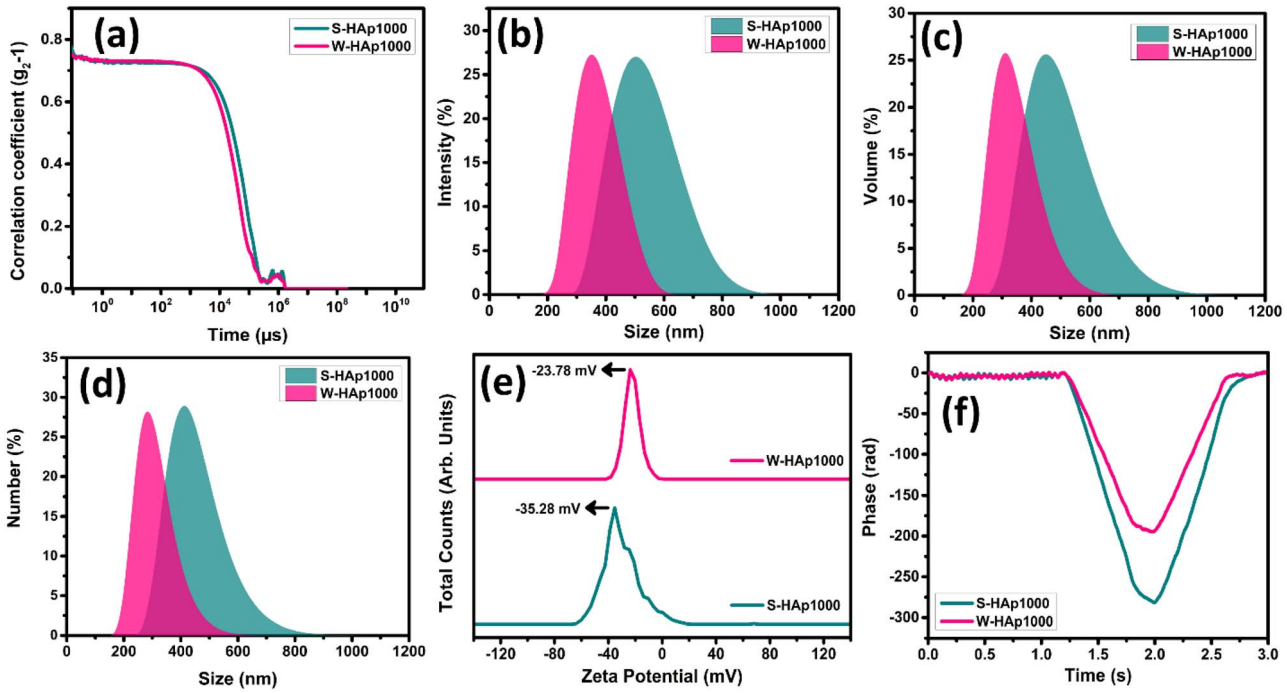

Fig. 7 Plots of particle size and surface charge analysis of the synthesized S-HAp1000 and W-HAp1000 samples: (a) correlogram; (b–d) intensity, volume and number-based size distribution; (e) zeta potential; and (f) phase analysis light scattering (PALS).

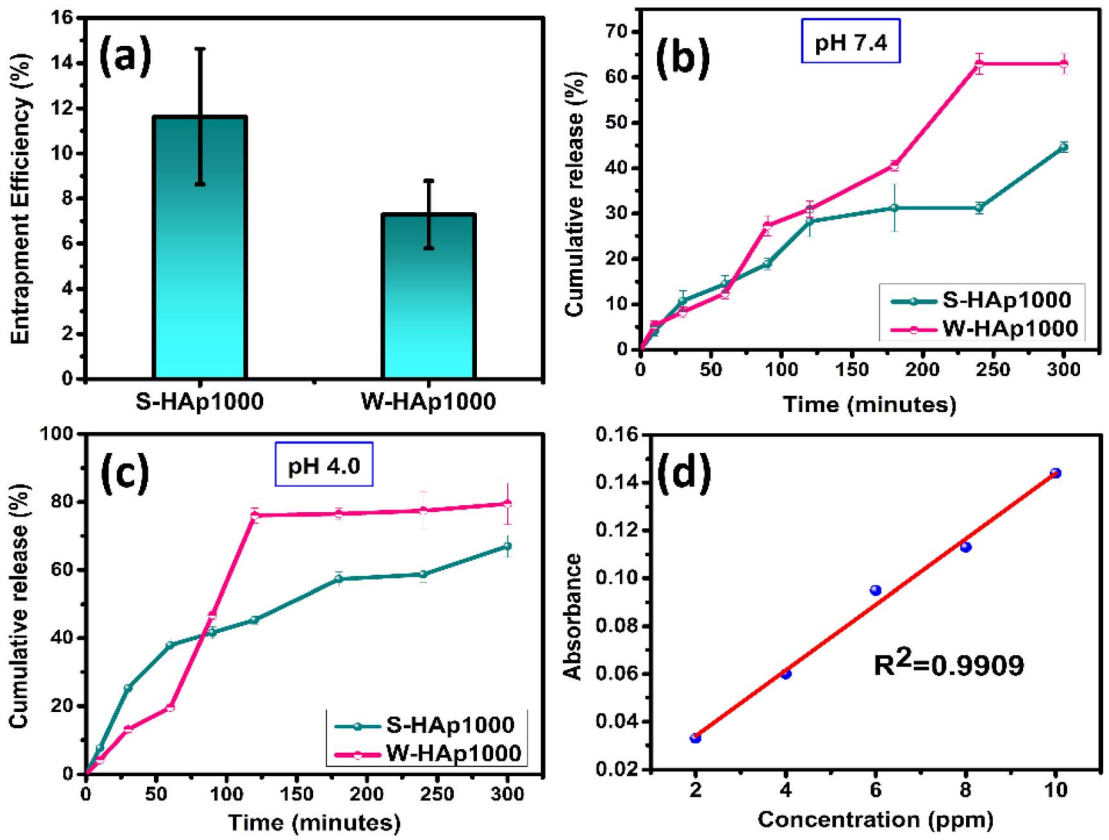

Fig. 8 (a) Entrapment efficiency for the loading of amoxicillin; *in vitro* release of amoxicillin in (b) pH 7.4 and (c) pH 4.0 from S-HAp1000 and W-HAp1000 samples; (d) calibration curve.

3.5. Analysis of particle size and surface charge

Along with the FESEM and TEM-based size analysis, dynamic light scattering (DLS) and zeta potential analysis were also carried out. The DLS-size analysis reveals distinct particle size characteristics for both S-HAp1000 and W-HAp1000 samples. The correlograms (Fig. 7a) display a typical exponential decay patterns that confirms successful particle size measurements through DLS technique. Based on the intensity, volume, and number-based size distribution plots (Fig. 7b–d), W-HAp1000 exhibits a relatively narrower and smaller particle size distribution compared to S-HAp1000. The intensity-based distribution shows that W-HAp1000 has a dominant peak around 360 nm, whereas S-HAp1000 displays a peak at around 488 nm. Similar results were also present in the volume and number-based distributions, indicating that the wet-chemically derived HAp possesses finer and more uniform particles.

The zeta potential analysis (Fig. 7e) reveals that both samples possess negative surface charges, with S-HAp1000 exhibiting a higher negative zeta potential of −35.28 mV compared to W-HAp1000 at −23.78 mV. This difference in surface charge indicates that the particles of the HAp samples have different stability in suspension, where higher negative zeta potential values typically associate with better colloidal stability due to stronger electrostatic repulsion between particles. The phase analysis light scattering (PALS) plots (Fig. 7f) show characteristic saw-tooth patterns at lower time frames, indicating good data quality for electrophoretic mobility measurements.

3.6. Assessment of *in vitro* drug release

The drug release behavior of S-HAp1000 and W-HAp1000 was investigated in SBF solution at two different pH conditions (7.4 and 4.0) to assess their potential as amoxicillin carriers.

The drug loading efficiency assessment (Fig. 8a) revealed that S-HAp1000 exhibited higher amoxicillin incorporation efficiency (11.63%) compared to W-HAp1000 (7.28%), which may be due to differences in their structural features. Drug release studies were conducted over 300 minutes at RT, and the cumulative release profiles showed strong pH dependence (Fig. 8b–d). At physiological pH 7.4 after 300 minutes, W-HAp1000 (62.96%) demonstrated higher drug release than S-HAp1000 (44.66%), indicating enhanced diffusion and weaker drug–carrier interactions in W-HAp1000. Under acidic conditions (pH 4.0), which mimic infection or inflammation sites, both materials exhibited accelerated release, with W-HAp1000 reaching over 79% cumulative release and S-HAp1000 reaching approximately 66%. The enhanced release at low pH is attributed to the protonation of amoxicillin and increased solubility, along with possible partial dissolution of HAp.[50,51] Based on this assessment, S-HAp1000 with a higher loading capacity and slower release has the potential for being used in sustained delivery applications, while W-HAp1000, offering faster and pH-responsive release, shows promise for targeted drug delivery in acidic pathological environments.

3.6.1. Release kinetic study. Understanding the kinetics of drug release is essential to interpret how materials like HAp interact with the encapsulated therapeutic agents and to evaluate their suitability for delivery systems. Kinetic modeling helps reveal the release mechanism whether it is governed by diffusion, matrix erosion, swelling, or a combination phenomenon.[52,53] By fitting experimental data to various kinetic models, the dominant release pathways can be elucidated which also helps in to compare the materials' behavior under physiological (pH 7.4) and pathological (pH 4.0) conditions.

The release kinetics of amoxicillin from the S-HAp1000 and W-HAp1000 samples were evaluated using four commonly applied mathematical models: zero-order, first-order, Higuchi,

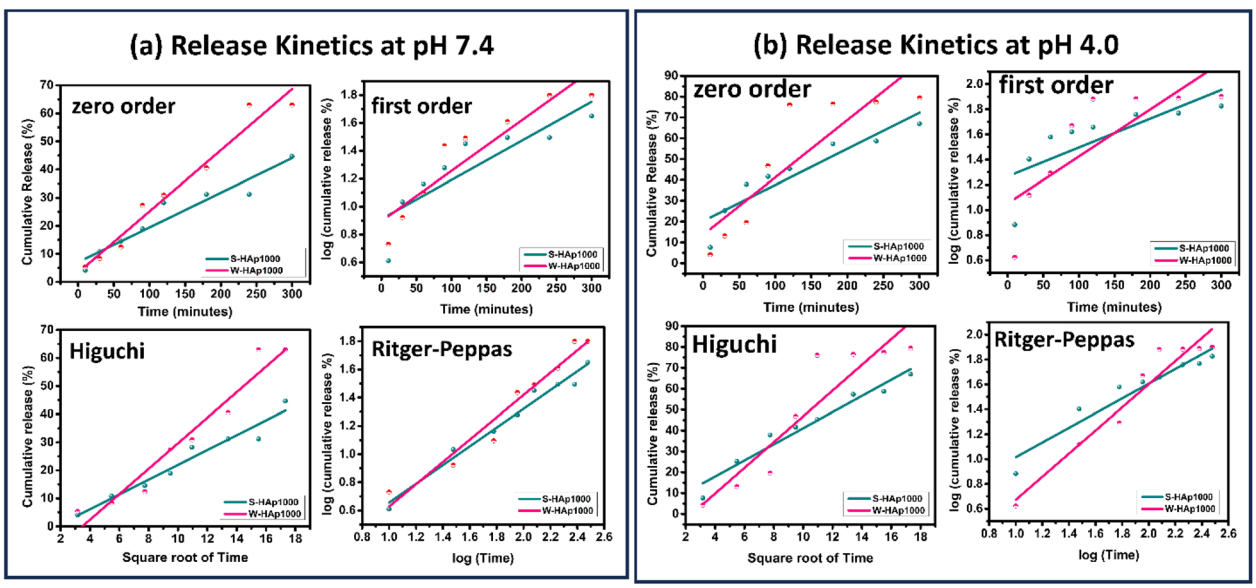

Fig. 9 Release kinetics of amoxicillin from S-HAp1000 and W-HAp1000 samples at (a) pH 7.4 and (b) pH 4.0 in SBF solution. Linear fitting of zero order, first order, Higuchi, and Ritger–Peppas kinetic model plots are presented for both of the samples.

Table 4 Results of kinetic model fitting for amoxicillin release in SBF solution from S-HAp1000 and W-HAp1000 samples at pH 7.4 and 4.0

Sample	Release pH condition	Zero order model		First order model		Higuchi model		Ritger–Peppas model		
		K_o	R^2	K_1	R^2	K_H	R^2	K_{KP}	n	R^2
S-HAp1000	7.4	0.123	0.912	0.0012	0.708	2.640	0.944	0.990	0.665	0.973
W-HAp1000		0.218	0.959	0.0016	0.837	4.547	0.938	0.848	0.792	0.949
S-HAp1000	4.0	0.173	0.829	0.0009	0.533	3.865	0.948	1.528	0.591	0.913
W-HAp1000		0.276	0.726	0.0016	0.596	6.169	0.841	0.773	0.929	0.929

Table 5 Results of antibacterial activity assessment of the amoxicillin loaded HAp samples by agar well diffusion assay[a]

Zone of inhibition in cm			
Sample	Concentration	*Staphylococcus aureus* (ATCC 29737)	*E. coli* (ATCC 11229)
S-HAp1000	0.1 mg mL^{-1}	1.1 ± 0.15	—
	0.2 mg mL^{-1}	1.4 ± 0.18	—
	0.3 mg mL^{-1}	1.5 ± 0.22	—
	0.4 mg mL^{-1}	1.4 ± 0.16	—
	0.5 mg mL^{-1}	1.6 ± 0.25	—
W-HAp1000	0.1 mg mL^{-1}	0.9 ± 0.19	—
	0.2 mg mL^{-1}	1.0 ± 0.20	0.9 ± 0.17
	0.3 mg mL^{-1}	1.3 ± 0.28	1.1 ± 0.16
	0.4 mg mL^{-1}	1.4 ± 0.15	1.1 ± 0.23
	0.5 mg mL^{-1}	1.4 ± 0.21	1.2 ± 0.21
Positive control	30 μg	2.5 ± 0.16	1.8 ± 0.50
Negative control	—	—	—

[a] "—" indicates no zone of inhibition.

and Ritger–Peppas models. Each of these models offers a different perspective on the release mechanism. The zero-order model assumes a constant release rate independent of drug concentration and desirable for uniform drug delivery. The first-order model describes a concentration-dependent release, while the Higuchi model interprets release as a diffusion-driven process from a homogeneous matrix. The Ritger–Peppas model, often used for polymeric or complex systems, characterizes the release mechanism based on the diffusional exponent n, with values indicating Fickian diffusion ($n \leq 0.45$), anomalous (non-Fickian) transport ($0.45 < n < 0.890$), or case II transport dominated by matrix relaxation or erosion ($n \geq 0.89$).[7,19] Fig. 9 represents the plots of linear fitting of the kinetic models that were employed for understanding the release behavior of amoxicillin from S-HAp1000 and W-HAp1000 samples at pH 7.4 and pH 4.0 in SBF solution and Table 4 lists the results of kinetic fittings.

At physiological pH 7.4, S-HAp1000 showed the best model fit with the Ritger–Peppas model ($R^2 = 0.973$), indicating that the release mechanism involves anomalous transport which is a combination of diffusion and matrix relaxation. The value of the release exponent ($n = 0.665$) further supports the existence within the non-Fickian range. In comparison, W-HAp1000 displayed the highest R^2 value (0.959) for the zero-order model. This indicates a more sustained and concentration-independent release profile although fitting with Ritger–Peppas model ($R^2 = 0.949$) further substantiates the existence of anomalous transport ($n = 0.792$). This suggests that both the diffusion of amoxicillin through the HAp matrix and structural changes in the material influence release behavior.

Under acidic conditions (pH 4.0), drug release was significantly enhanced due to the increased solubility of HAp and the protonation of amoxicillin.[54] S-HAp1000 fit best with the Higuchi model ($R^2 = 0.948$), indicating a dominant diffusion-controlled process in this environment. The corresponding value of n ($n = 0.591$) from the Ritger–Peppas model fitting confirms anomalous transport, although the slightly lower R^2 value (0.913) suggests a minor deviation from the ideal model behavior. W-HAp1000 on the other hand, followed the Ritger–Peppas model most closely ($R^2 = 0.929$), which indicates a transition to case II transport, dominated by polymer relaxation or matrix erosion mechanisms.

By controlling the synthesis parameters, such as the synthesis route, calcination temperature, and precursor concentration, it is possible to precisely tailor the material's properties including its crystallinity, porosity, and surface area to achieve the desired release profile for a particular clinical application. For instance, in cases of acute osteomyelitis, a rapid, high-concentration dose of antibiotics is often required to effectively combat a sudden bacterial surge. The W-HAp1000 material is ideal for this purpose, as it demonstrated a faster and more efficient release of amoxicillin, releasing up to 62.96% at pH 7.4 and 79.18% at pH 4.0. This burst release is beneficial for achieving a high local antibiotic concentration to quickly eliminate the pathogen.

On the other hand, chronic infections, such as those associated with implant failure, require a sustained, long-term therapeutic drug level to prevent a recurrence. In this case, the S-HAp1000 sample is more suitable due to its slower and more prolonged release profile, releasing only 44.66% at pH 7.4 and 66.01% at pH 4.0. This controlled release minimizes systemic exposure and maintains a therapeutic concentration at the infection site over an extended period.

3.7. Antibacterial activity and cytocompatibility assessment

The antibacterial activity of the amoxicillin-loaded HAp samples was evaluated across a range of concentrations. The findings demonstrated that both samples were capable of inhibiting

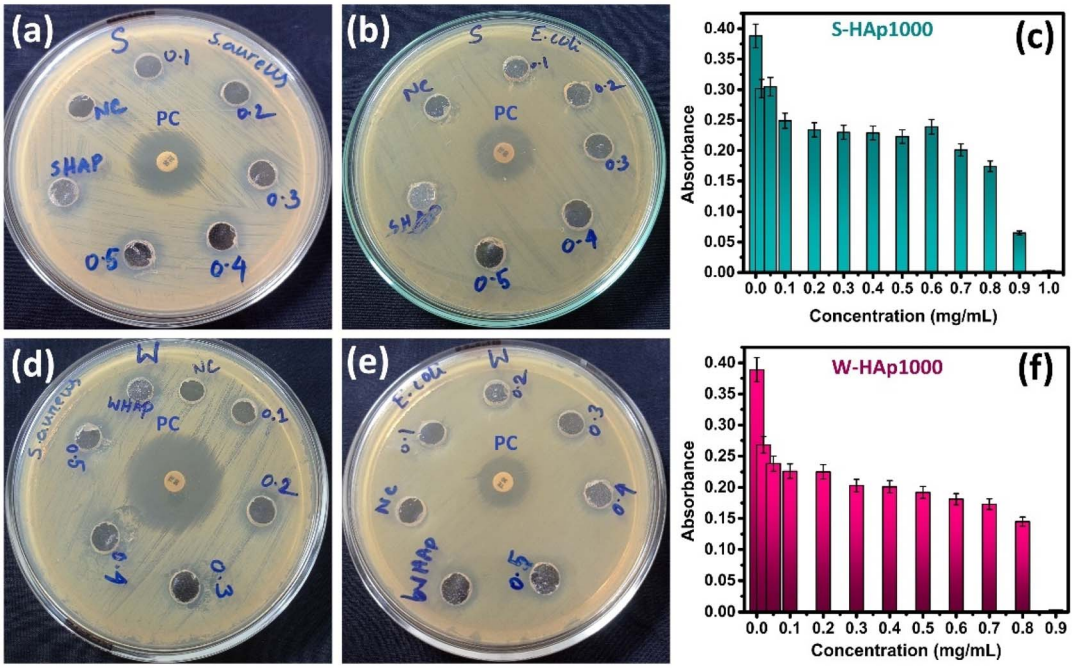

Fig. 10 Antibacterial activity of amoxicillin-loaded (a and b) S-HAp1000 and (d and e) W-HAp1000 against *Staphylococcus aureus* and *Escherichia coli* at different concentrations. Absorbance data at 600 nm for MIC and MBC determination against *Staphylococcus aureus* is presented for (c) S-HAp1000 and (f) W-HAp1000. Tetracycline disc was used as positive control and DMSO solvent as negative control. 'PC' = positive control; 'NC' = negative control.

bacterial growth, although the extent of activity varied depending on the material and bacterial strain.

According to the presented data of Table 5 and the Fig. 10, the amoxicillin-loaded S-HAp1000 exhibited the highest inhibitory effect against *S. aureus* at a concentration of 0.5 mg mL^{-1}, producing a zone of inhibition measuring 1.6 ± 0.25 cm. However, no visible inhibition zone was observed against *E. coli* at any tested concentration. In contrast, the amoxicillin-loaded W-HAp1000 at 0.5 mg mL^{-1} showed antibacterial activity against both *S. aureus* (1.4 ± 0.21 cm) and *E. coli* (1.2 ± 0.21 cm). The probable reasons for S-HAp1000 not being able to inhibit *E. coli*, despite having higher amoxicillin content, may be due to its limited drug release that can cause inadequate availability of drug required for inhibition. Additionally, stronger matrix-drug binding and unfavorable surface properties may also add to S-HAp1000's inability to inhibit *E. coli* at this given concentration. On the other hand, W-HAp1000's broader activity, despite lower loading, reflects more effective drug release and potentially advantageous surface characteristics, overcoming even the natural resistance barrier of Gram-negative bacteria. The positive control (tetracycline) displayed substantial zones of inhibition against both bacterial strains, while the negative control (DMSO) exhibited no antibacterial effect.

The minimum inhibitory concentration (MIC) and minimum bactericidal concentration (MBC) were determined specifically against *S. aureus*, due to its critical role in osteomyelitis pathogenesis. The S-HAp1000 sample showed an MIC of 0.1 mg mL^{-1}, with an MBC of 1.0 mg mL^{-1} (Fig. 10c). Similarly, the W-HAp1000 sample exhibited an MIC at the same concentration (0.1 mg mL^{-1}), while its MBC was slightly lower, at 0.9 mg mL^{-1} (Fig. 10f).

The cytocompatibility assessment using Vero cells demonstrated that both amoxicillin-loaded S-HAp1000 and W-HAp1000 samples exhibited excellent biocompatibility, with cell viability values exceeding 95% after 24 h of incubation. These results indicate that neither the HAp matrices nor the released amoxicillin exerted any significant cytotoxic effects on Vero cells under the tested conditions. In comparison, both the positive and negative solvent controls maintained 100% viability, confirming the reliability of the assay. The high survival rate observed for the drug-loaded samples highlights the biosafety of the developed carriers and supports their potential application in localized antibiotic delivery for bone-related infections.

4 Conclusion

This study demonstrates that the method of HAp synthesis plays a crucial role in defining its drug delivery characteristics. Solid-state synthesized S-HAp1000 achieved higher drug loading due to greater crystallinity and larger crystallite size, making it more suited for sustained release applications. In contrast, W-HAp1000, prepared by wet chemical precipitation, offered faster and pH-responsive amoxicillin release, enabled by its phase purity, finer particle size, and greater surface accessibility. Although S-HAp1000 had higher amoxicillin content, its limited release resulted in no activity against *E. coli*, unlike W-HAp1000, which exhibited broad-spectrum antibacterial

action. The drug release kinetics further highlight mechanistic differences: diffusion-dominated in S-HAp1000 *versus* relaxation- or erosion-driven release in W-HAp1000. These results indicate that wet chemical precipitation is more effective for applications requiring responsive and efficient delivery, while solid-state HAp may be reserved for long-term, controlled drug administration. This work emphasizes the need to tailor synthesis strategies according to the intended drug delivery function, particularly in the context of treating localized bone infections like osteomyelitis.

Author contributions

Mashrafi Bin Mobarak: conceptualization, methodology, resources, funding acquisition, project administration, formal analysis, investigation, data curation, writing – original draft, writing – review & editing. Sumaya Tabassum: methodology, investigation, data curation. Md Sohag Hossain: investigation, data curation. Nourin Tarannum: methodology, investigation, data curation, writing – original draft. Fariha Chowdhury: formal analysis, investigation, data curation. Md. Sahadat Hossain: formal analysis. Nazmul Islam Tanvir: formal analysis. Samina Ahmed: supervision, resources.

Conflicts of interest

There is no conflict to declare.

Data availability

All data supporting the findings of this study are included in the main manuscript. Additional raw data are available from the corresponding author upon reasonable request.

Supplementary information: Rietveld-refined XRD patterns of the synthesized HAp sample. See DOI: **https://doi.org/10.1039/d5ra06021d**.

Acknowledgements

This study was financially supported by the Ministry of Science and Technology (MoST), Government of the People's Republic of Bangladesh (Ref. No. 39.00.0000.012.02.010.24-42; Date: 04/03/2025; Project ID: 2430293; SL No. 293 ASE). Additional support was provided by the Bangladesh Council of Scientific and Industrial Research (BCSIR) under its R&D project initiative (R&D reference no. 39.02.0000.011.14.169.2023/877; Date: 17/09/2023).

References

1 S. Sultana, M. S. Hossain, M. Mahmud, M. B. Mobarak, M. H. Kabir, N. Sharmin and S. Ahmed, *RSC Adv.*, 2021, **11**, 3686–3694.
2 A. S. Shalfia Judit, R. Feyolah Herin, S. Sebastiammal, J. Henry, M. Santhosh and M. Santhamoorthy, *Phosphorus, Sulfur Silicon Relat. Elem.*, 2025, **200**, 12–36.
3 H. Lee, G. Han, Y. Na, M. Kang, S.-J. Bang, H. S. Kang, T.-S. Jang, J.-H. Park, H. L. Jang, K. Yang, H. Kang and H.-D. Jung, *Adv. Funct. Mater.*, 2024, **34**, 2406237.
4 M. S. Hossain, M. M. Hasan, M. Mahmud, M. B. Mobarak and S. Ahmed, *Chem. Pap.*, 2023, **77**, 463–471.
5 S.-W. Lee, S.-G. Kim, C. Balázsi, W.-S. Chae and H.-O. Lee, *Oral Surg. Oral Med. Oral Pathol. Oral Radiol.*, 2012, **113**, 348–355.
6 D. Shankar, K. Jayaganesh, N. Gowda, K. S. Lakshmi, K. J. Jayanthi and S. C. Jambagi, *Biomater. Adv.*, 2024, **158**, 213791.
7 M. B. Mobarak, M. N. Islam, F. Chowdhury, M. N. Uddin, M. S. Hossain, M. Mahmud, U. S. Akhtar, N. I. Tanvir, A. M. Rahman and S. Ahmed, *RSC Adv.*, 2023, **13**, 36209–36222.
8 N. M. Pu'ad, P. Koshy, H. Z. Abdullah, M. I. Idris and T. C. Lee, *Heliyon*, 2019, **5**(5), e01588.
9 M. B. Mobarak, M. S. Hossain, Z. Yeasmin, M. Mahmud, M. M. Rahman, S. Sultana, S. M. Masum and S. Ahmed, *J. Mol. Struct.*, 2022, **1252**, 132142.
10 I.-S. Kim and P. N. Kumta, *Mater. Sci. Eng., B*, 2004, **111**, 232–236.
11 P. Feng, R. Zhao, L. Yang, S. Chen, D. Wang, H. Pan and C. Shuai, *Ceram. Int.*, 2022, **48**, 33682–33692.
12 A. Cüneyt Tas, *Biomaterials*, 2000, **21**, 1429–1438.
13 M. B. Mobarak, M. N. Uddin, F. Chowdhury, M. S. Hossain, M. Mahmud, S. Sarkar, N. I. Tanvir and S. Ahmed, *J. Mol. Struct.*, 2024, **1301**, 137321.
14 G. Qian, L. Xiong and Q. Ye, *RSC Adv.*, 2023, **13**, 16512–16528.
15 S. Tabassum, S. Zahid, F. Zarif, M. A. Gilani, F. Manzoor, F. Rehman, A. Jamal, A. A. Chaudhry, S. A. Siddiqi and I. ur Rehman, *RSC Adv.*, 2016, **6**, 104969–104978.
16 S. Sebastian, J. Huang, Y. Liu, F. Tandberg, M. Collin, M. Puthia and D. B. Raina, *J. Orthop. Res.*, 2024, **42**, 212–222.
17 A. Mele, L. Gjurgjaj, J. Lica, A. Mema, A. Mele, I. Çaçani, F. Keraj, F. Baldassarre and D. Siliqi, *Dent. Mater.*, 2023, **39**, e43.
18 M. Sadat-Shojai, M.-T. Khorasani, E. Dinpanah-Khoshdargi and A. Jamshidi, *Acta Biomater.*, 2013, **9**, 7591–7621.
19 M. B. Mobarak, F. Chowdhury, M. N. Uddin, M. S. Hossain, U. Akhtar, N. I. Tanvir, M. A. A. Shaikh and S. Ahmed, *Mater. Adv.*, 2024, **5**, 9716–9730.
20 S. S. A. Abidi and Q. Murtaza, *J. Mater. Sci. Technol.*, 2014, **30**, 307–310.
21 W. Xue, X. Liu, X. Zheng and C. Ding, *J. Biomed. Mater. Res., Part A*, 2005, **74A**, 553–561.
22 W. Suchanek and M. Yoshimura, *J. Mater. Res.*, 1998, **13**, 94–117.
23 R. Z. LeGeros, *Clin. Mater.*, 1993, **14**, 65–88.
24 A. Ogose, T. Hotta, H. Kawashima, N. Kondo, W. Gu, T. Kamura and N. Endo, *J. Biomed. Mater. Res., Part B*, 2005, **72B**, 94–101.
25 A. Hogan, V. G. Heppert and A. J. Suda, *Arch. Orthop. Trauma Surg.*, 2013, **133**, 1183–1196.
26 S. Mondal, S. V. Dorozhkin and U. Pal, *Wiley Interdiscip. Rev. Nanomed. Nanobiotechnol.*, 2018, **10**, e1504.

27 H. Dym and J. Zeidan, *Dent. Clin. North Am.*, 2017, **61**, 271–282.
28 N. Haddad, J. Ajaz, L. Mansour, R. Kasemodel, J. Jarvis, J. Jarad, H. Gorski and M. Carr, *Antibiotics*, 2024, **13**, 4.
29 M. B. Mobarak, N. S. Pinky, F. Chowdhury, M. S. Hossain, M. Mahmud, M. S. Quddus, S. A. Jahan and S. Ahmed, *J. Saudi Chem. Soc.*, 2023, 101690.
30 A. C. Tas, *Biomaterials*, 2000, **21**, 1429–1438.
31 T. Kokubo, H. Kushitani, S. Sakka, T. Kitsugi and T. Yamamuro, *J. Biomed. Mater. Res.*, 1990, **24**, 721–734.
32 T. Saha, M. B. Mobarak, M. N. Uddin, M. S. Quddus, M. R. Naim and N. S. Pinky, *Mater. Chem. Phys.*, 2023, 127979.
33 F. Chowdhury, M. B. Mobarak, M. Hakim, M. N. Uddin, M. S. Hossain, U. S. Akhter, D. Islam, S. Ahmed and H. Das, *New J. Chem.*, 2024, **48**, 17038–17051.
34 M. Sohag Hossain, S. Alam Aumi, N. Tarannum, F. Chowdhury, M. S. Hossain, M. Farid Ahmed, N. Islam Tanvir, U. Sarmeen Akhtar, S. Ahmed and M. Bin Mobarak, *RSC Adv.*, 2025, **15**, 30564–30575.
35 M. B. Mobarak, F. Chowdhury and S. Ahmed, *RSC Adv.*, 2024, **14**, 39874–39889.
36 M. B. Mobarak, S. A. Fahim, M. S. Hossain, F. Chowdhury, N. I. Tanvir, U. S. Akhtar and S. Ahmed, *ACS Sustainable Resour. Manage.*, 2025, acssusresmgt.5c00244.
37 W.-F. Ho, H.-C. Hsu, S.-K. Hsu, C.-W. Hung and S.-C. Wu, *Ceram. Int.*, 2013, **39**, 6467–6473.
38 V. Rodríguez-Lugo, T. V. K. Karthik, D. Mendoza-Anaya, E. Rubio-Rosas, L. S. Villaseñor Cerón, M. I. Reyes-Valderrama and E. Salinas-Rodríguez, *R. Soc. Open Sci.*, 2018, **5**, 180962.
39 H. Murata, R. Kawanabe, A. Tada, Y. Tokudome and A. Nakahira, *J. Ceram. Soc. Jpn.*, 2023, **131**, 17–21.
40 M. S. Hossain, M. Mahmud, S. Sultana, M. Bin Mobarak, M. S. Islam and S. Ahmed, *R. Soc. Open Sci.*, 2021, **8**, 210684.
41 G. B. Harris, *London, Edinburgh Dublin Phil. Mag. J. Sci.*, 1952, **43**, 113–123.
42 G. V. Tendeloo, O. I. Lebedev, M. Hervieu and B. Raveau, *Rep. Prog. Phys.*, 2004, **67**, 1315.
43 M. Kumar, A. Kumar and A. C. Abhyankar, *RSC Adv.*, 2015, **5**, 35704–35708.
44 A. G. Matveeva, T. S. Skripkina, V. M. Nekrasov, U. E. Nikiforova, V. A. Bukhtoyarov, A. Bychkov and I. Lomovskiy, *Powder Technol.*, 2025, **449**, 120370.
45 C. J. Wilcock, P. Gentile, P. V. Hatton and C. A. Miller, *J. Vis. Exp.*, 2017, e55343.
46 L. O. Ahmed and R. A. Omer, *Rev. Inorg. Chem.*, 2024, **44**, 599–618.
47 M. S. Hossain, M. A. A. Shaikh, S. A. Jahan, M. Mahmud, M. B. Mobarak, M. S. Rahaman, M. N. Uddin and S. Ahmed, *RSC Adv.*, 2023, **13**, 9654–9664.
48 J. Barralet, S. Best and W. Bonfield, *J. Biomed. Mater. Res.*, 1998, **41**, 79–86.
49 M. S. Hossain, M. S. Hossain, S. Ahmed and M. B. Mobarak, *RSC Adv.*, 2024, **14**, 38560–38577.
50 F. Crea, D. Cucinotta, C. De Stefano, D. Milea, S. Sammartano and G. Vianelli, *Eur. J. Pharm. Sci.*, 2012, **47**, 661–677.
51 R. Das Mahapatra, A. Jo, K. B. Cahaya Imani, J.-W. Chung and J. Yoon, *Polym. Chem.*, 2022, **13**, 5234–5242.
52 V. Uskoković, *J. Mater. Chem. B*, 2019, **7**, 3982–3992.
53 I. J. Macha, B. Ben-Nissan and W. H. Müller, *Key Eng. Mater.*, 2017, **758**, 113–119.
54 L. Gu, X. He and Z. Wu, *Mater. Chem. Phys.*, 2014, **148**, 153–158.